SANDIA REPORT
SAND2010-3258
Unlimited Release
Printed May 2010

Fourier Analysis and Synthesis Tomography

Daniel Feldkuhn and Kelvin Wagner

Report prepared by Michael B Sinclair

Prepared by
Sandia National Laboratories
Albuquerque, New Mexico 87185 and Livermore, California 94550

Sandia National Laboratories is a multi-program laboratory operaterd by Sandia Corporation, a wholly owned subsidiary of Lockheed Martin Corperation, for the U. S. Department of Energy's National Nuclear Security Administration under Contract DE-AC04-94AL85000.

Sandia National Laboratories

Issued by Sandia National Laboratories, operated for the United States Department of Energy by Sandia Corporation.

Available to DOE and DOE contractors from
U.S. Department of Energy
Office of Scientific and Technical Information
P.O. Box 62
Oak Ridge, TN 37831

Telephone: (865) 576-8401
Facsimile: (865) 576-5728
E-Mail: reports@adonis.osti.gov
Online ordering: http://www.osti.gov/bridge

Available to the public from
U.S. Department of Commerce
National Technical Information Service
5285 Port Royal Rd.
Springfield, VA 22161

Telephone: (800) 553-6847
Facsimile: (703) 605-6900
E-Mail: orders@ntis.fedworld.gov
Online order: http://www.ntis.gov/help/ordermethods.asp?loc=7-4-0#online

SAND2010-3258
Unlimited Release
Printed May 2010

Fourier Analysis and Synthesis Tomography

Daniel Feldkuhn and Kelvin H Wagner
Electrical and Computer Engineering Department
University of Colorado at Boulder
Boulder, CO, 80309

report prepared by:
Michael B Sinclair
Sandia National Laboratories
Albuquerque, NM 87185

Abstract

Most far-field optical imaging systems rely on a lens and spatially-resolved detection to probe distinct locations on the object. We describe and demonstrate a novel high-speed wide-field approach to imaging that instead measures the complex spatial Fourier transform of the object by detecting its spatially-integrated response to dynamic acousto-optically synthesized structured illumination. Tomographic filtered backprojection is applied to reconstruct the object in two or three dimensions. This technique decouples depth-of-field and working-distance from resolution, in contrast to conventional imaging, and can be used to image biological and synthetic structures in fluoresced or scattered light employing coherent or broadband illumination. We discuss the electronically programmable transfer function of the optical system and its implications for imaging dynamic processes. Finally, we present for the first time two-dimensional high-resolution image reconstructions demonstrating a three-orders-of-magnitude improvement in depth-of-field over conventional lens-based microscopy.

Intentionally Left Blank

Contents

Figures

1 Preface

This SAND report describes the technical accomplishments that were supported by a Campus Executive Graduate Fellowship Laboratory Directed Research and Development (LDRD) award to Daniel Feldkuhn at the University of Colorado at Boulder. The LDRD award funded the development of the Fourier Analysis and Synthesis Tomography (FAST) microscope during fiscal years 2007 and 2008. This report contains the text of a manuscript prepared by Daniel Feldkuhn describing the theory, construction, and operation of the FAST microscope.

2 Introduction

Conventionally, "imaging" implies a process wherein a visual likeness of an object is formed by sensing some of its characteristics, such as color and reflectivity, at distinct points in space. However, while such spatial basis decomposition is an intuitive way to represent and measure structure, in many situations other representations can be advantageous. Holographic systems, for example, capture the three-dimensional structure of an object indirectly by interferometrically recording the phase and amplitude of a scattered optical wavefront [1]. Alternatively, measurements of the far-field diffraction patterns created by an object under coherent illumination can be used not only to characterize its texture, but also to extract its large-scale and small-scale three-dimensional structure using diffraction tomography [2] or speckle interferometry [3] techniques without relying on an imaging lens. On the other hand, the resolution of conventional lens-based wide-field imaging systems can be enhanced beyond the diffraction limit by illuminating the object with a sequence of patterns and applying spatial heterodyne algorithms to the resulting images [4, 5]. In applications where available bandwidth is highly constrained or in wavelength regimes where detector arrays are expensive or not available, it is possible to optically encode a two-dimensional image into a compressed data stream by spatially modulating the object wavefront with a series of pseudorandom binary patterns and detecting the resulting light flux using a high-speed single-element detector [6]. Spatially integrating detection is also employed in optical scanning holography in combination with rapidly-moving structured illumination and heterodyne processing of the time-domain signal, resulting in a laser-based imaging system characterized by an incoherent point spread function [7]. In this paper, we will describe a new approach to wide-field image formation that shares many common elements with these various techniques, such as spatial and temporal heterodyne detection, tomographic reconstruction, structured illumination, single-element sensing, compressive imaging, and an incoherent optical transfer function, yet provides unique capabilities for measuring two- and three-dimensional structures [8, 9, 10].

Using the Fourier Theorem, a three-dimensional (3D) structure can be decomposed into a linear sum of sinusoids. If the 3D object is illuminated by plane waves from many directions and we disregard multiple scattering (according to the first Born approximation), each Fourier component acts much like a sinusoidal volume grating, diffracting a pair of planar wavefronts, whose orientations, amplitudes, relative phases, and relative angular separation are determined by the orientation, amplitude, phase, and spatial frequency of the Bragg-matched volume grating [13, 14, 11]. As illustrated in Figure 1, the fundamental role of lenses in an imaging system is to capture this emitted angular spectrum of plane waves [15] and recombine it at the image plane, creating a linear superposition of interference patterns that form the image. However, because the Numerical Aperture (NA) of the objective lens limits the angular range of captured plane waves, the lens acts as a low-pass filter in the Fourier domain, limiting the optical resolution. Note also that phase errors varying across the lens apertures produce phase and amplitude errors in the image that depend on spatial frequency. We will refer to the linear effects of the optical system on the spatial frequency components of the structure being imaged as the Optical Transfer Function (OTF). Furthermore, we can map the orientation, amplitude, and phase of the plane waves captured by the imaging system to complex points distributed in a volume of the three-dimensional Fourier space, as illustrated in Figure 2. In this

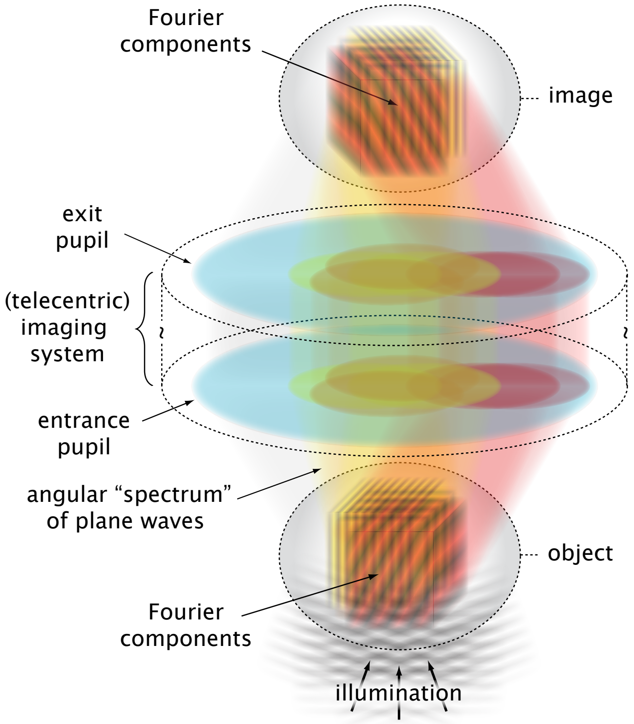

Figure 1. Image formation through Fourier decomposition and synthesis by a telecentric lens-based imaging system represented by an entrance and exit pupil. Colors represent different spatial Fourier components, rather than different wavelengths.

representation, the out-of-plane points are due to diffraction from tilted Fourier components of the object structure and limit the depth-of-field (DOF) of the optical system, which is found to vary inversely with the square of the NA. These observations also extend to more complex optical systems, in which the entrance and exit pupils play the role of lens apertures.

Unlike lens-based imaging systems which simultaneously process a volume of points in Fourier space, we will describe an imaging technique that rapidly measures individual complex Fourier coefficients of the object. Such Fourier basis decomposition not only makes it possible to decouple DOF from NA by planar sampling of Fourier space, but also offers great flexibility in dynamically controlling the OTF. Although Fourier-domain imaging systems have been proposed in the context of microscopy [16, 17] and remote target characterization using Fourier Telescopy [18, 19], they have remained largely unexplored in practice due to limited speed and precision of mechanical scanning systems. More recently, a hybrid fluorescent imaging technique has been demonstrated combining sparse Fourier basis decomposition without mechanical scanning with high-speed low-resolution lens-based imaging to enhance the resolution of a conventional microscope [20, 21, 22, 23]. Building on these bodies of work, we have developed a new approach to Fourier-domain imaging: Fourier Analysis and Synthesis Tomography (FAST).

3 Fundamentals of FAST

The basic principle of FAST has its roots in a simple observation: the spatially-integrated flux scattered, fluoresced, or transmitted by an object that is illuminated by a moving sinusoidal pattern will oscillate in time, the amplitude and phase of the oscillation corresponding to the strength and offset of the

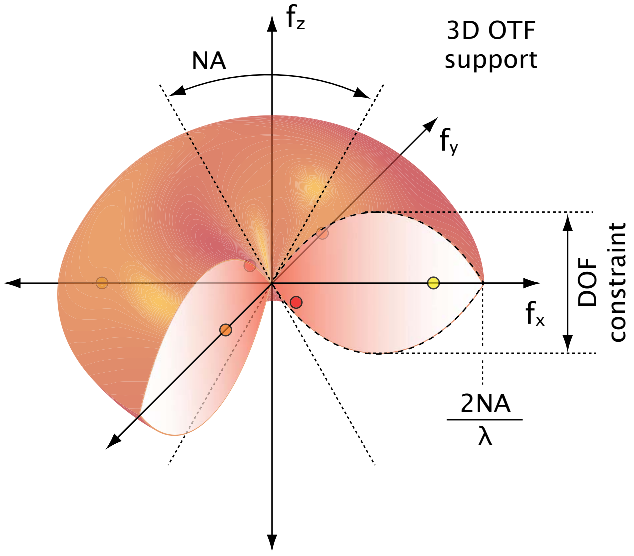

Figure 2. The three-dimensional OTF support of a spatially-incoherent lens-based imaging system under the first Born approximation, representing the range of spatial frequencies captured by the aperture [11, 12] (colored circles show the spatial frequencies illustrated in Figure 1). The aperture acts as a low-pass filter with a spatial frequency cut-off at $\sim 2NA/\lambda$. The finite aperture results in a "missing cone" of spatial frequencies in the Fourier domain, with the cone angle equal to the NA. The Depth Of Field varies as λ/NA^2 and is determined by the extent of the OTF in the f_z dimension.

matching Fourier component present in the intensity response of the object. For the 2D case, this can be seen mathematically by decomposing the intensity response of the structure being measured into its Fourier components, multiplying by a moving sinusoidal intensity pattern, and spatially integrating:

$$\begin{aligned} I_d(t) = I_i \iint_{\infty}^{\infty} & \left[\iint_{\infty}^{\infty} \mathcal{I}_r(f_x, f_y) e^{j2\pi(f_x x + f_y y)} df_x df_y \right] \\ & \times \left[1 + \frac{m}{2} e^{j2\pi(f_{0x} x - \nu_0 t)} + c.c. \right] dx dy \\ = I_i & \Big(\mathcal{I}_r(0,0) + \frac{m}{2} \mathcal{I}_r(f_{0x}, 0) e^{j2\pi\nu_0 t} + c.c. \Big) \ . \end{aligned} \tag{1}$$

Here $\mathcal{I}_r(f_x, f_y)$ represents the complex Fourier transform of the intensity response of the structure encompassed by the finite illumination area, I_i and I_d are the incident and detected intensities, f_{0x} and ν_0 are the spatial and temporal frequencies of the illumination, m is the modulation depth, and *c.c.* represents the complex conjugate. Thus, by illuminating the object with a sequence of moving sinusoidal fringes spanning a range of spatial frequencies and orientations, detecting the spatially-integrated response with a single-element detector, and demodulating the time-domain signal, the intensity image can be recovered by Fourier synthesis.

Since the number of Fourier samples collected in this manner determines the number of degrees of freedom in the image, each Fourier sample must be measured in a matter of microseconds or faster to make this approach a practical alternative to pixel-based or spot-scanning techniques [24]. Figure 3a illustrates the key elements of FAST that make this possible. Instead of mechanical scanning, FAST uses an acousto-optic Bragg cell to spatially modulate the illumination wavefront. Here we will consider bulk acousto-optic spatial modulation of visible light [25], however other high-speed spatial modulator technologies such as a reflective SAW device [26] or a grating light valve [27] can be used with FIR, UV, or potentially even X-ray illumination. In the low-efficiency linear diffraction regime, a pair of tones driving

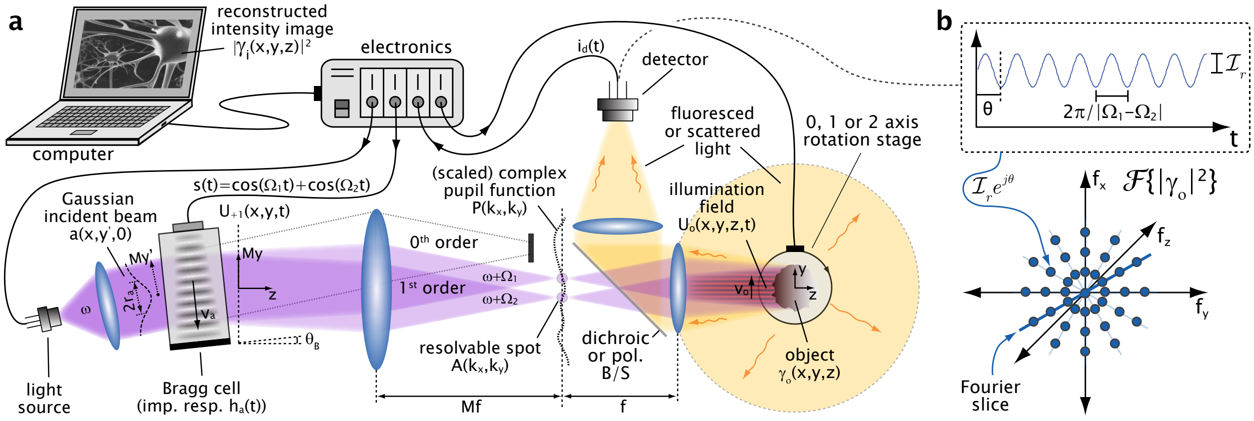

Figure 3. **(a)** The key optical elements of acousto-optic FAST. A two-tone RF drive signal diffracting two 1^{st} order beams is illustrated for clarity, however $s(t)$ and the diffracted 1^{st} order field can be more complex. **(b)** A running fringe pattern produces a modulated detector signal, its amplitude and phase corresponding to the complex Fourier coefficient at the spatial frequency of the fringes. A spectrum of such fringe patterns measures a slice through the object's 3D Fourier space.

the Bragg cell creates a pair of 1st-order diffracted wavefronts. By optically projecting the acoustic field propagating in the Bragg cell onto the object, the diffracted wavefronts are made to interfere, producing sinusoidal fringes running across the object at the projected acoustic velocity and with a pitch proportional to the two-tone beat frequency. Thus, by driving the Bragg cell with a double-sided chirp, for example, the object is probed with a succession of spatial frequencies, thereby measuring a linear slice through Fourier space, as illustrated in Figure 3b. For a Bragg cell, the maximum number of resolvable Fourier samples along the slice is limited by the time-bandwidth product (TB), while the minimum sample time is dictated by the acoustic propagation time (t_a). For a high-resolution device with TB ∼1000 and t_a ∼10 us, it takes ∼10 ms to measure 1000 Fourier samples (assuming the detector and the digitizer can keep up). Additional Fourier slices can be measured by rotating the object or rotating the illumination pattern using a prism [28, 29] or an arrangement of mirrors. We are also investigating several non-mechanical illumination rotation designs that are capable of fully rotating the illumination pattern faster than the acoustic access time, t_a, and could increase the imaging speed by several orders of magnitude [30].

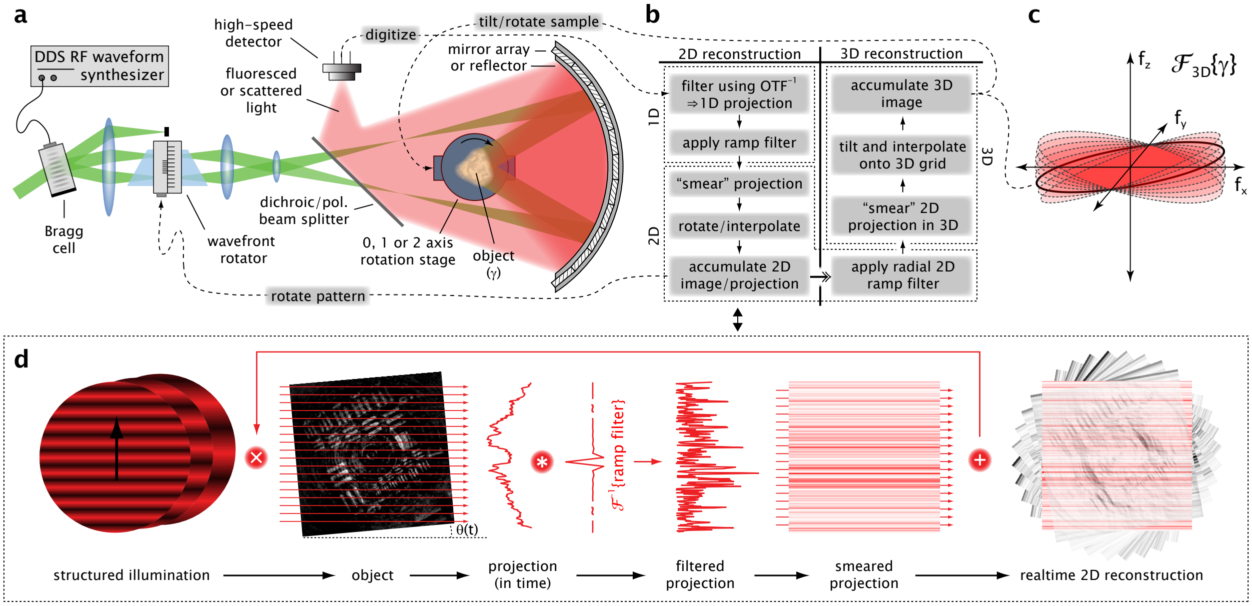

Figure 4. **(a)** A reflective implementation of FAST. The acousto-optically diffracted first-order beams are rotated using a prism or other means and projected as plane waves onto the sample using a large NA and working-distance optic (coarse phase errors in the optic can be compensated electronically). The sample can be tilted and/or rotated to access different Fourier planes for 3D measurements. The modulated light fluoresced or scattered from the object is collected with high efficiency onto a high-speed detector, whose signal is tomographically processed to reconstruct the object. **(b)** Key steps in two and three-dimensional image synthesis by filtered backprojection. **(c)** Tilted-plane sampling of Fourier space makes 3D reconstruction possible using a three-dimensional extension of the Fourier Slice Theorem. **(d)** A real-space picture of filtered backprojection: A two-dimensional object is decomposed into (time-domain) one-dimensional projections using structured illumination. Each projection is filtered with a ramp filter to compensate for radial sampling and "smeared" along the projection axis. The smeared backprojections are summed to build up a two-dimensional image in real time, projection-by-projection.

3.1 Extended Depth of Field

Note that whereas the spatial resolution of the system is limited by the NA of the projection system, the DOF depends only on the axial extent of the fringe pattern. As a result, FAST can resolve wavelength-scale features while maintaining a millimeter-scale DOF (e.g. see illumination field in Figure 3a). This resolution-independent DOF is a manifestation of planar sampling of Fourier space inherent in two-dimensional imaging with sequential FAST. Furthermore, by tilting the object relative to the illumination one can measure additional tilted planes in the Fourier domain and thereby reconstruct three-dimensional structures – without rejecting light as in confocal optical sectioning. As illustrated in Figure 4a, due to the direct mapping between projection aperture coordinates and Fourier space, it is also possible to use a large low-precision high-NA reflector, or even a mosaic of flat mirrors positioned at a distance from the object to both, project high spatial frequency structured illumination, and collect as much of the light from the object as possible. As we will show, coarse phase errors in the reflector can be compensated electronically via the acoustic waveform or in post-processing. We are currently developing such a phase-compensated system using a large electroformed metal reflector with NA of ∼0.4 and a working distance of 20 cm.

3.2 Tomographic Image Synthesis

Since for each Fourier slice the temporal frequencies comprising the detector signal correspond to spatial Fourier coefficients of the object, the time-domain signal can be considered as a one-dimensional projection of the object structure filtered by the one-dimensional point-spread-function of the system. Hence, in analogy to projection tomography techniques [31, 2], the image synthesis task is to reconstruct multi-dimensional structure from a series of one-dimensional projections. To accomplish this, the well-known tomographic filtered backprojection algorithm [2] can be applied in two or three dimensions to the digitized and filtered detector signal as illustrated in Figure 4b-d. This algorithm can be used to form the image in real time, slice by slice, and is less sensitive to registration artifacts than rectilinear direct Fourier transform methods.

3.3 Frequency-Multiplexed Sampling

Our discussion so far has focused on sequential Fourier sampling, however the throughput of FAST can be increased further by driving the Bragg cell with many tones simultaneously, creating a superposition of running fringe patterns with different spatial frequencies at the object. Due to the acousto-optic Doppler shift, each spatial frequency maps to a different carrier frequency in the spectrum of the detector signal. Hence, the simultaneous Fourier-domain measurements are readily separable and the same Fourier synthesis methods used with sequential sampling apply. In photon-rich conditions, such frequency-multiplexed (FM) Fourier sampling allows measurement of an entire Fourier slice during the acoustic propagation time (t_a ∼10 us). One drawback of FM sampling is that due to the inherent presence of frequency-redundant tilted interference patterns DOF and NA are no longer decoupled. This disadvantage can be mitigated by using a hybrid approach that sequentially combines FM measurements spanning narrow frequency "bins". Another solution that maintains the speed advantage of FM sampling without sacrificing DOF (but trades sensitivity and flexibility in OTF synthesis) is double-sided non-redundant FM sampling. This approach as well as other sampling strategies are illustrated in Figure 5.

4 Dynamic Optical Transfer Function

More generally, referring to Figure 3a, consider the effect of an arbitrary RF signal, $s(t)$, driving the Bragg cell on the detector current, $i_d(t)$, when an object with a fluorescent intensity response, $|\gamma_o(x, y, z)|^2$, is illuminated by spatially and temporally coherent light (i.e. CW laser light). It is first helpful to make some reasonable simplifying assumptions: the illumination system projecting the acoustic pattern onto the object is linear and space-invariant with a magnification M^{-1}; the collimated source beam is uniform and has a Gaussian field profile $a(x, y')$ with a beam waist radius of $r_a = Mr_o$ along the Mx and My'

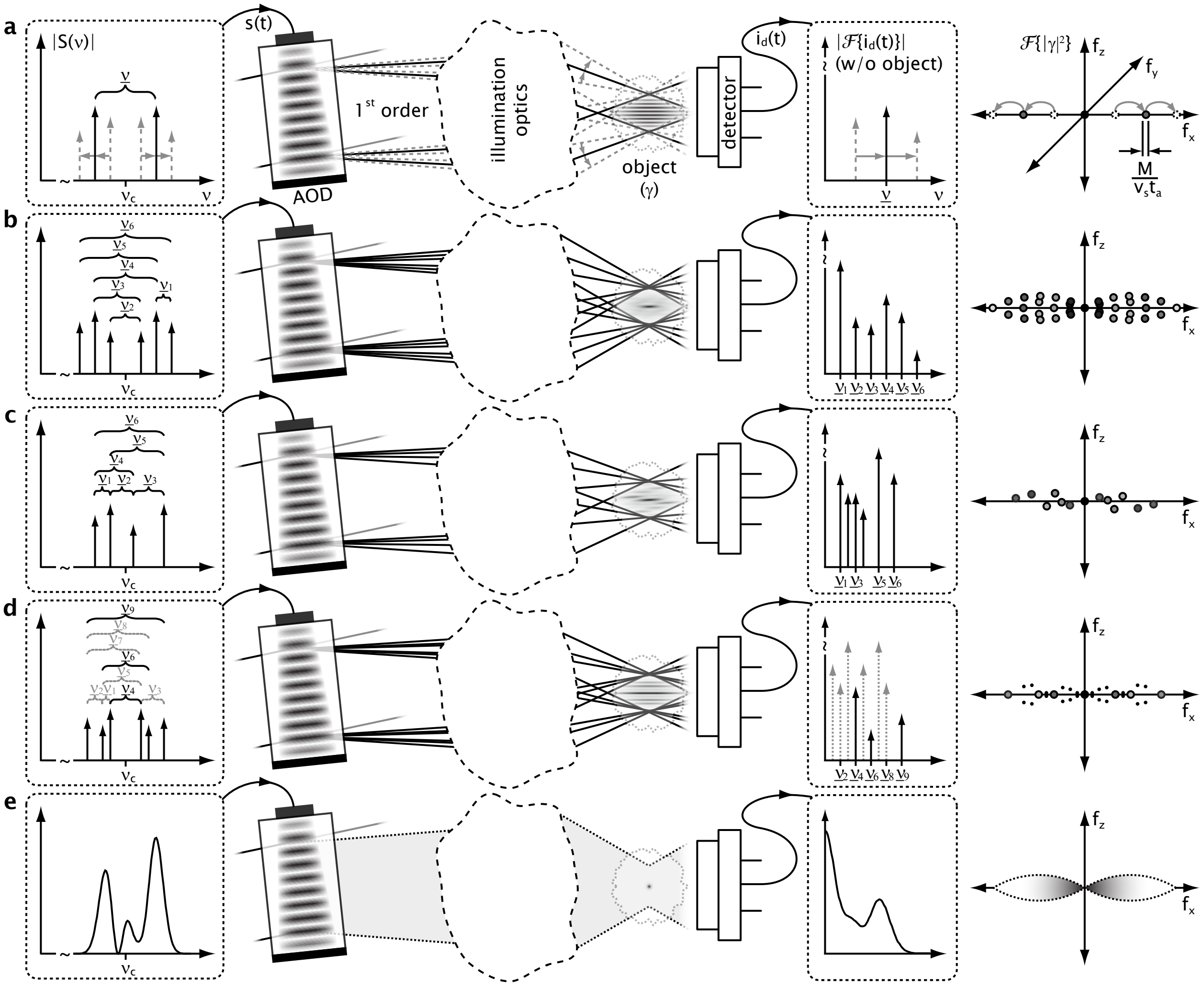

scaled by 80%

Figure 5. **(a)** Time-multiplexed (sequential) sampling. The object is illuminated with one fringe pattern at a time resulting in a large DOF. Period, amplitude, phase, and orientation of illumination pattern may be chosen independently for each sample (dashed/dotted lines represent past/future samples). Fourier sample resolution is determined by the acousto-optic access time, t_a, scaled by velocity of sound v_s and magnification, M, of illumination optics. **(b)** Frequency-multiplexed (FM) sampling. The object is illuminated with multiple spatial frequencies to measure multiple samples along a Fourier slice simultaneously, thereby speeding up the measurement. However, the DOF is reduced due to coherent contributions from several redundant tilted interference patterns at each spatial frequency. **(c)** Non-redundant FM sampling. Since there are no redundant beats in the RF signal, each detected carrier maps to a distinct Fourier sample, however the samples are not collinear. **(d)** Double-sided non-redundant FM sampling. Symmetric RF tone pairs produce non-redundant beats, while signal contributions due to redundant tilted interference patterns at other frequencies are rejected (dotted gray impulses, small dots in Fourier space). The remaining samples lie along a Fourier slice resulting in a large DOF at the cost of reduced signal strength. **(e)** Continuous FM sampling. A continuous RF spectrum can be used to measure an entire Fourier slice with a reduced DOF. The OTF (for one slice) is an autocorrelation of the RF spectrum with t_a-limited frequency resolution and spans a figure-8 pattern in the $f_x - f_z$ plane.

dimensions; the incident field is modulated by the Bragg cell only in the $y - z$ plane; the Bragg cell is driven relatively weakly so that the diffracted optical power depends linearly on the RF power; and the linear polarization of the interfering beams is always normal to the plane of beam propagation. We also neglect device-specific polarization dependence of the acousto-optic interaction and acoustic energy walk-off [32]. Furthermore, we make the Fresnel (paraxial) approximation in calculating diffracted fields using Fourier transform techniques. Although this approximation is not accurate for high-NA illumination patterns, paraxial analysis offers much insight into the fundamental optical properties of FAST.

The RF waveform, $s(t)$, driving the Bragg cell can be written as a complex signal, $s_m(t)$, modulating a carrier oscillating at the angular center frequency, Ω_c: $s(t) = s_m(t)e^{-j\Omega_c t} + c.c.$ By treating the Bragg cell as a tilted moving phase grating and assuming linear diffraction, it can be shown [15] that the complex amplitude of the $+1^{st}$-order acousto-optically diffracted field, $U_{+1}(x, y, t)$ can be written approximately as:

$$U_{+1}(x, y, t) \propto a(x, y) s_a\left(t + \frac{y}{v_o}\right) e^{-j\omega_+ t} + c.c.\ , \tag{2}$$

where

$$s_a\left(t + \frac{y}{v_o}\right) \equiv h_a(t) \circledast s_m(t) \circledast \delta\left(t - \frac{t_a}{2} + \frac{My}{v_a}\right). \tag{3}$$

Here $\circledast$ stands for temporal convolution, v_a is the acoustic velocity in the Bragg crystal, $v_o = v_a/M$ is the demagnified fringe velocity, $\omega_+ = \omega + \Omega_c$ is the Doppler up-shifted optical frequency, and $U_i(x, y, t) = a(x, y)e^{-j\omega t}$ is the complex amplitude of the incident optical field. The term $h_a(t)$ is the acousto-optic impulse response. It represents the Fourier transform of the electro-acousto-optic bandshape (downshifted to baseband) and incorporates effects such as frequency-dependent diffraction efficiency and the electronic frequency response of the Bragg cell [32]. The acoustic beat signal, $s_a(t + y/v_o)$, represents the scaled and carrier-demodulated traveling index of refraction perturbation within the Bragg cell. A delay of one half of the acousto-optic access time, t_a, is included since the coordinate system origin is centered in the middle of the beam [25]. The linear phase factor, $e^{jk_0 y\theta_B}$, due to the Bragg angle, θ_B, is not explicitly written since it is canceled by the tilt between the y and y' axes.

The three-dimensional field, $U_o(x, y, z, t)$, illuminating the object, can be found by convolving the diffracted field with the 2D point spread function, $p_i(x, y)$, of the illumination optical system, and propagating the resulting two-dimensional field in z using the free space propagator, $h_0(x, y, z)$:

$$U_o(x, y, z, t) = U_{+1}(x, y, t) ** p_i(x, y) ** h_0(x, y; z), \tag{4}$$

where $**$ stands for 2D spatial convolution. It is also helpful to write the *k-space* representation of the illumination field by taking a 2D Fourier transform (parameterized by z and t):

$$\begin{aligned}
\mathcal{F}_{xy}\left\{U_o\right\} &\propto \left[A(k_x, k_y) * S_a(k_y v_o) e^{jk_y v_o t}\right] \\
&\quad \times P_i(k_x, k_y) H_0(k_x, k_y; z) e^{-j\omega_+ t} + c.c. \\
&= e^{-j\omega_+ t} \int_{-\infty}^{\infty} A(k_x, k_y - \kappa) \\
&\quad \times \left[e^{jk_0 z} e^{-j(k_x^2 + k_y^2)z/2k_0}\right] \\
&\quad \times P_i(k_x, k_y) S_a(\kappa v_o) e^{j\kappa v_o t} d\kappa + c.c.\ .
\end{aligned} \tag{5}$$

Here $k_0 = 2\pi/\lambda_0$ is the free-space optical wave-vector, k_x and k_y are its planar components, $*$ stands for 1D spatial convolution, the upper-case letters represent the Fourier transforms of the corresponding lower-case functions, and the bracketed term is the Fresnel approximation of the free space transfer function, $H_0(k_x, k_y; z)$ [15]. As illustrated in Figure 3a, the term $A(k_x, k_y - \kappa)$ corresponds to the Fourier plane spot due to a diffracted beam, while the integration variable, $\kappa \equiv \Omega_m/v_o$, represents the offset of the diffracted spot in the Fourier plane and depends on the respective angular frequency component, Ω_m, in the RF modulation signal, $s_m(t)$. The term $P_i(k_x, k_y) = |P_i(k_x, k_y)|e^{j\Delta\phi(k_x, k_y)}$ is the complex pupil function of the illumination system incorporating phase errors, $\Delta\phi(k_x, k_y)$, due to various aberrations in the optical system [15], as illustrated by the curve at the Fourier plane in Figure 3a.

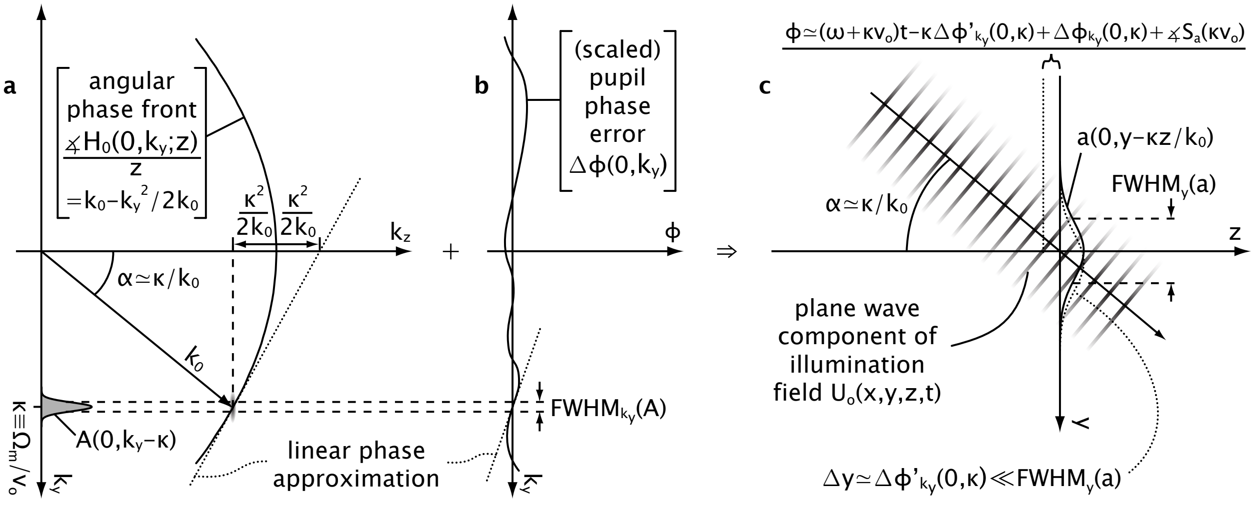

Figure 6. **(a)** The ideal paraxial angular phase front due to the Fresnel propagator, $H_0(0,k_y;z)$, can be linearized in the small neighborhood encompassed by the spot function, $A(0,k_y-\kappa)$. **(b)** Since the pupil phase error function varies much slower than the angular phase front, it can be similarly linearized (note: the phase error function is greatly exaggerated relative to the angular phase front). **(c)** The linearized phase functions result in a linear combination of tilted and phase-shifted plane waves under a Gaussian envelope illuminating the object. Note that a slight y-shift of the Gaussian envelope due to the linear term of the phase error function is negligible compared to the envelope size.

By making several key Fourier-domain approximations according to Figure 6 and transforming back to real space, the illumination field can be written as:

$$\begin{aligned} U_o(x,y,z,t) &\propto e^{j(k_0 z - j\omega_+ t)} \\ &\times \int_{-\infty}^{\infty} e^{-j\kappa(y - v_o t - z\kappa/2k_0)} a\Big(x, y - \frac{\kappa z}{k_0}\Big) \\ &\times \Big[e^{-j\kappa\Delta\phi'_{k_y}(0,\kappa)} P_i(0,\kappa) S_a(\kappa v_o)\Big]\, d\kappa + c.c.\ . \end{aligned} \tag{6}$$

As illustrated in Figure 6c, in this form the illumination field is seen to be a superposition of moving, tilted, phase-shifted plane waves, where each plane wave has a tilted Gaussian envelope and is modulated by the product of the complex-valued pupil function and the RF spectrum evaluated at the corresponding RF modulation angular frequency $\kappa \equiv \Omega_m/v_o$. Thus, it is clear even at this point in the analysis that it is possible to correct any linear phase error affecting the diffraction spot in the pupil plane at a given κ by electronically adjusting the spectrum of the RF modulation signal, $s_m(t)$.

To find the relation between the illumination field and the detected signal, we first observe that since the far-field radiation due to each fluorophore is nearly isotropic and incoherent with respect to other fluorophores, the fluoresced light captured by the objective and integrated on the detector is proportional to the total fluorescent flux from the object. Thus, ignoring DC bias and optical-frequency terms, the *time-varying* portion of the detector signal, $\tilde{i}_d(t)$, can be found by multiplying the time-varying illumination intensity by the object's fluorescent intensity response, $|\gamma_o(x, y, z)|^2$, and spatially integrating in 3D:

$$\tilde{i}_d(t) \propto \iiint_{-\infty}^{\infty} |\gamma_o(x, y, z)|^2 \bigg| \int_{-\infty}^{\infty} e^{-j\kappa(y - z\kappa/2k_0)} \times a\Big(x, y - \frac{\kappa z}{k_0}\Big) P_S(\kappa v_o) e^{j\kappa v_o t} d\kappa \bigg|^2 dxdydz, \tag{7}$$

where $P_S(\kappa v_o)$ represents the modulated pupil function expressed by the bracketed term in Equation 6. Remembering that $a(x, y - \kappa z/k_0)$ represents a tilted Gaussian beam envelope, recognizing the argument of the magnitude-squared operator as an inverse temporal Fourier transform, and employing the autocorrelation theorem, the Fourier transform of the time-varying detector signal can be written as:

$$\begin{aligned} \mathcal{F}_t\left\{\tilde{i}_d(t)\right\} \propto & \iiint_{-\infty}^{\infty} dxdydz \\ & \times |\gamma_o(x, y, z)|^2 e^{-(x^2+y^2)/r_o^2} e^{-j\Omega_m y/v_o} \\ & \times \mathcal{R}_{\Omega_m}\left\{ e^{(j-2z/r_o^2 k_0)\Omega_m^2 z/2k_0 v_o^2} e^{2\Omega_m z y/r_o^2 k_0 v_o} P_S(\Omega_m) \right\}, \end{aligned} \tag{8}$$

where

$$P_S(\Omega_m) = e^{-j\Delta\phi'_{k_y}(0,\Omega_m/v_o)\Omega_m/v_o} \times P_i\left(0, \frac{\Omega_m}{v_o}\right) S_m(\Omega_m) H_a(\Omega_m) e^{-j\Omega_m t_a/2}. \tag{9}$$

Here, we have made the substitution $\kappa \equiv \Omega_m/v_o$, used $\mathcal{R}_{\Omega_m}\{\}$ to represent autocorrelation in Ω_m, and expanded $P_S(\Omega_m)$ with the help of Equations 3 and 6 ($H_a(\Omega_m)$ represents the acousto-optic transfer function).

We can simplify and interpret Equation 8 in terms of a 1D OTF when the modulation signal, $s_m(t)$, is either a single tone used for sequential Fourier sampling or a wide-band waveform as in the case of frequency-multiplexed Fourier sampling.

4.1 The 1D OTF for Sequential Fourier Sampling

The modulated pupil function, $P_S(\Omega_m)$ due to a complex single-tone signal, $s_m(t)$, with a frequency, Ω_0, can be expressed as an impulse pair:

$$P_S(\Omega_m; \Omega_0) = P_S(\Omega_0)\delta(\Omega_m - \Omega_0) + P_S(-\Omega_0)\delta(\Omega_m + \Omega_0), \tag{10}$$

where $\delta()$ is a Dirac delta function, while $P_S(\Omega_0)$ and $P_S(-\Omega_0)$ represent the complex amplitudes of the positive and negative sidebands. In this case, the autocorrelation term in Equation 8 can be simplified, and the Fourier transform of the time-varying detector signal can be written as:

$$\begin{aligned} \mathcal{F}_t\left\{\tilde{i}_d(t)\right\} \propto & \iiint_{-\infty}^{\infty} |\gamma_o(x, y, z)|^2 e^{-(x^2+y^2)/r_o^2} \\ & \times e^{-2(\Omega_0 z/r_o k_0 v_o)^2} dxdz e^{-j\Omega_m y/v_o} dy \\ & \times \big[P_S(\Omega_0) P_S^*(-\Omega_0)\delta(\Omega_m + 2\Omega_0) \\ & \quad + P_S^*(\Omega_0) P_S(-\Omega_0)\delta(\Omega_m - 2\Omega_0)\big]. \end{aligned} \tag{11}$$

The bracketed term corresponds to the autocorrelation of the modulated pupil function without the DC term (which we have explicitly neglected by considering only the time-varying detector signal). We represent this DC-filtered autocorrelation by $\tilde{\mathcal{R}}_{\Omega_m}\{P_S(\Omega_m; \Omega_0)\}$. One may also recognize the inner double-integral as a y-axis projection operator and the outer integral as a Fourier transform. To interpret this result we map temporal to spatial dimensions using $t \mapsto y/v_o$ and $\Omega_m \mapsto k_y v_o$ (a key step in processing the digitized detector signal), obtaining:

$$\begin{aligned}\mathcal{F}\left\{\tilde{i}_d(t)\right\} &= \int_{-\infty}^{\infty} \tilde{i}_d(t) e^{-j\Omega_m t} dt \\ &\longmapsto \int_{-\infty}^{\infty} \tilde{i}_d\left(\frac{y}{v_o}\right) e^{-jk_y y} dy = \mathcal{F}_y\left\{\tilde{i}_d\left(\frac{y}{v_o}\right)\right\}, \end{aligned} \tag{12}$$

such that

$$\begin{aligned}\mathcal{F}_y\left\{\tilde{i}_d\left(\frac{y}{v_o}\right)\right\} &\propto \mathcal{F}_y\Big\{\mathcal{P}_y\Big\{|\gamma_o(x,y,z)|^2\Big[e^{-(x^2+y^2)/r_o^2} \\ &\times e^{-2(\Omega_0 z/r_o k_0 v_o)^2}\Big]\Big\}\Big\}\tilde{\mathcal{R}}_{\Omega_m}\{P_S(\Omega_m;\Omega_0)\}, \end{aligned} \tag{13}$$

where $\mathcal{P}_y$ is a y-axis projection operator. We can see from this expression that before projection onto the y-axis, the object's intensity response is windowed by a Gaussian function along each dimension. The 3D Gaussian window, $w(x, y, z, \Omega_0)$, represented by the term in square brackets, corresponds to the intensity envelope of the interference pattern illuminating the object. The 2D Gaussian envelope in the $x - y$ plane limits the field of view, while the z-dependent Gaussian function limits the depth of field.

The autocorrelation in Equation 13 can be interpreted as a transfer function by mapping the time-domain detector signal to a 1D projection of the intensity image. By utilizing the Fourier Slice Theorem [33], the 1D OTF, $H_{1D}(\Omega_m; \Omega_0)$, relating a slice through the 3D Fourier space of the windowed object to a Fourier slice of the image for the case of single-tone RF modulation can now be obtained:

$$\begin{aligned}\mathcal{F}_y\left\{\tilde{i}_d(y/v_o)\right\} &\equiv \mathcal{F}_y\left\{\mathcal{P}_y\left\{|\gamma_i(x,y,z)|^2\right\}\right\} \\ &= \mathcal{SF}_{k_y}\left\{|\gamma_o(x,y,z)|^2 w(x,y,z,\Omega_0)\right\} H_{1D}(\Omega_m;\Omega_0), \end{aligned} \tag{14}$$

where

$$\begin{aligned}H_{1D}(\Omega_m;\Omega_0) &= \tilde{\mathcal{R}}_{\Omega_m}\{P_S(\Omega_m;\Omega_0)\} \\ &= P_S(\Omega_0)P_S^*(-\Omega_0)\delta(\Omega_m + 2\Omega_0) \\ &+ P_S^*(\Omega_0)P_S(-\Omega_0)\delta(\Omega_m - 2\Omega_0). \end{aligned} \tag{15}$$

Here $P_S(\Omega_m; \Omega_0)$ is given by Equations 9 and 10, the operator $\mathcal{SF}_{k_y}$ takes a 1D Fourier slice along the k_y axis of the 3D Fourier transform of the operand, and as before, $\Omega_m \mapsto k_y v_o$.

The 1D OTF expression in Equation 15 applies to measuring a single spatial Fourier component of the windowed object. It is also possible to formulate a synthetic 1D OTF characterizing the sequential measurement of an entire Fourier slice by varying the modulation frequency, Ω_0. However, since the depth extent of the Gaussian window function, $w(x, y, z, \Omega_0)$, in Equation 14 varies with frequency, in order to describe the measurement using a space-invariant synthetic OTF one must assume that the depth of the object of interest is substantially smaller than the depth of field over the full frequency range of the measurement and treat the window function as constant in z. Using Equation 13 and scaling between Bragg cell space and object space using the demagnification factor, M, the waist radius of the Gaussian window in z can be written as:

$$r_z = \frac{r_a v_a}{\sqrt{2}M^2\lambda_0\nu_0}, \tag{16}$$

where $\nu_0 = \Omega_0/2\pi$ is the RF frequency. We can think of r_z as a measure of the depth of field of sequential FAST.

As an example, for a FAST system with $M = -20$, $r_a = 10$: , $v_a = 620$: , $\lambda_0 = 0.5$: , $(\nu_m)_{max} = 10$: MHz, and $\mathrm{NA}_{max} = 0.16$, the minimum depth of field, $(r_z)_{min}$, is approximately 2 mm. In this case, for a thin (sub-mm) microscopic object, the window function is approximately constant in z and

Ω_0 and the synthetic 1D-OTF for sequentially measuring N samples along a Fourier slice can be written as:

$$\begin{aligned} H_{1D}(\Omega_m) &\approx \frac{\mathcal{SF}_{k_y}\left\{|\gamma_i(x,y,z)|^2\right\}}{\mathcal{SF}_{k_y}\left\{|\gamma_o(x,y,z)|^2 w(x,y)\right\}} \\ &= \sum_{i=0}^{N} \tilde{\mathcal{R}}_{\Omega_m}\{P_S(\Omega_m;\Omega_i)\}. \end{aligned} \tag{17}$$

We can see from Equations 15 and 17 that by sequential Fourier sampling it is possible to synthesize an arbitrary 1D OTF function, as long as it exhibits conjugate inversion symmetry. With frequency-multiplexed sampling, on the other hand, the choice of the 1D OTF is much more constrained.

4.2 The 1D OTF for Frequency-Multiplexed Fourier Sampling

When the RF spectrum of the modulation signal, s_m, is broadband it is more challenging to interpret Equation 8, however we can proceed by noting that within a limited depth range about the focal plane, the y-dependent exponential term in the autocorrelation is approximately constant. If we assume that the edge of the field of view is located at a distance of r_o from the illumination axis, the y-dependent autocorrelation term can be neglected when:

$$z \ll \frac{r_a v_a}{2M^2\lambda_0\nu_m}. \tag{18}$$

For the example system parameters from the previous paragraph, the range constraint is found to be $z \ll 1.55$ mm and is applicable to many microscopic objects such as samples on a glass slide. Moreover, as will become apparent shortly, the depth of field of frequency-multiplexed FAST using a broadband modulation signal is much smaller than this range and the approximation is valid even for thick objects.

Mapping temporal to spatial dimensions using Equation 12 and neglecting the y-dependence of the autocorrelation, Equation 8 can now be written as:

$$\begin{aligned} &\mathcal{F}_y\left\{\tilde{\imath}_d(y/v_o)\right\} \\ &\quad\propto \int_{-\infty}^{\infty} \mathcal{F}_y\left\{\mathcal{P}_{yz}\left\{|\gamma_o(x,y,z)|^2\left[e^{-(x^2+y^2)/r_o^2}\right]\right\}\right\} \\ &\quad\quad\times \mathcal{R}_{\Omega_m}\left\{e^{(j-2z/r_o^2k_0)\Omega_m^2 z/2k_0v_o^2} P_S(\Omega_m)\right\} dz. \end{aligned} \tag{19}$$

The term in square brackets is the Gaussian window function, $w(x,y)$, and the $\mathcal{P}_{yz}$ operator projects the windowed 3D object intensity structure onto the $y-z$ plane. This expression can be interpreted by considering the object as a stack of thin 2D depth slices. The detector signal can then be treated as a superposition of y-axis projections of each 2D slice, each projection filtered by a different z-dependent 1D OTF, $H_{1D}(\Omega_m;z)$:

$$\begin{aligned} \mathcal{F}_y\left\{\tilde{\imath}_d(y/v_o)\right\} &\equiv \int_{-\infty}^{\infty} \mathcal{F}_y\left\{\mathcal{P}_{yz}\left\{|\gamma_i(x,y;z)|^2\right\}\right\} dz \\ &= \int_{-\infty}^{\infty} \mathcal{SF}_{k_yz}\left\{|\gamma_o(x,y;z)|^2 w(x,y)\right\} \\ &\quad\times H_{1D}(\Omega_m;z)dz, \end{aligned} \tag{20}$$

where

$$\begin{aligned} H_{1D}(\Omega_m;z) &= \frac{\mathcal{SF}_{k_yz}\left\{|\gamma_i(x,y;z)|^2\right\}}{\mathcal{SF}_{k_yz}\left\{|\gamma_o(x,y;z)|^2 w(x,y)\right\}} \\ &= \mathcal{R}_{\Omega_m}\left\{e^{(j-2z/r_o^2k_0)\Omega_m^2 z/2k_0v_o^2} P_S(\Omega_m)\right\}. \end{aligned} \tag{21}$$

Here $P_S(\Omega_m)$ is defined in Equation 9, the $\mathcal{SF}_{k_yz}$ operator takes a 1D slice along the k_y axis of the 2D Fourier transform of the operand for each object depth, z, and $\Omega_m \mapsto k_y v_o$.

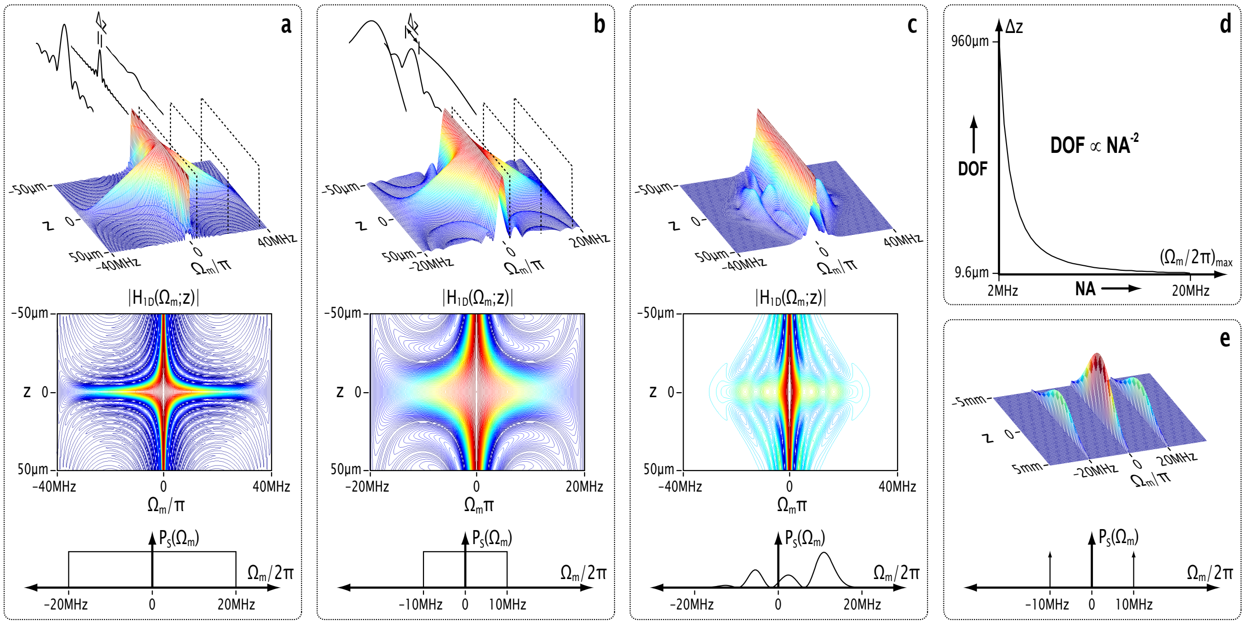

Figure 7. **(a)** Height and contour maps of the magnitude of the z-dependent 1D OTF of the specified example FAST system plotted using Equation 21. The modulation signal driving the Bragg cell has a flat-top RF spectrum spanning 20 MHz. The width of the illustrated sinc profiles, Δz, limits the depth of field at each frequency. The triangular OTF profile at $z = 0$ is the autocorrelation of the rectangular RF spectrum. Note that Δz has a minimum at half of the maximum frequency (the mid-frequency), in accordance with Figure 2. **(b)** Halving of the width of the RF spectrum quadruples the depth of field measure, Δz. **(c)** 1D OTF for an arbitrary asymmetric modulated pupil function amplitude profile. **(d)** The width of the main sinc lobe, Δz, at the mid-frequency is plotted as a function of RF spectral width (assuming a rect spectrum). Δz is found to vary quadratically with the inverse of frequency, corresponding to the quadratic dependence of DOF on the inverse of NA in conventional lens-based imaging systems. **(e)** A qualitative plot of the 1D OTF for a single-tone signal. Note that this plot slightly overestimates the depth of field since Equation 21 does not take into account the y-dependence of the OTF several millimeters away from the focal plane.

Figure 7 plots $|H_{1D}(\Omega_m; z)|$ for the example system parameters presented earlier and a modulation signal with a flat-top spectrum described by the rect function. Since in FAST there is a direct correspondence between the RF spectrum and a 1D slice through the pupil function, it is not surprising that a frequency-multiplexed FAST system with a rectangular RF spectrum shares many of the properties of a conventional *incoherent* optical system with a rectangular pupil function [15] (incoherent because intensity rather than field is detected). For example, at $z = 0$, the 1D OTF has a triangular pass-band, corresponding to the autocorrelation of the *rect* function. The width, Δz, of the main lobe of the sinc z-profile of the 1D OTF at each frequency, which is a measure of the local depth of field, is maximum at the lowest and highest frequencies and minimum at mid-frequencies, which is consistent with the illustration in Figure 2. Moreover, by plotting the minimum Δz as a function of RF bandwidth, it is clear that depth of field varies quadratically with the inverse of frequency, which is consistent with the inverse quadratic relationship between DOF and NA in conventional optical systems.

In contrast to traditional lens-based imaging, however, one of the strength of FAST is the ability to electronically synthesize a variety of 1D OTF phase and amplitude profiles that can lead to different trade-offs between DOF, resolution, and other degrees of freedom than in the case of the simple rectangular pupil function. Equation 21 allows one to calculate the depth-dependent behavior of the 1D-OTF of FAST near the focal plane for any Bragg cell modulation signal, $s_m(t)$. For example, Figure 7c plots the 1D OTF for an arbitrary asymmetric electronically synthesized pupil function profile, while Figure 7e plots the 1D OTF for a single-tone signal, which as we saw in the previous section leads to a nearly complete decoupling between depth of field and resolution. By comparing Equation 21 with Equation 8, however, it is evident that in the case of frequency-multiplexed sampling the synthetic 1D OTF is constrained to the form of a z-dependent autocorrelation function in contrast to the nearly arbitrary z-*independent* 1D-OTF that can be synthesized by sequential sampling. Nevertheless, even this constrained ability to electronically program the pupil function constitutes a powerful tool for controlling image formation. Moreover, it is possible to leverage both the measurement speed benefit of frequency-multiplexed sampling as well as the large depth of field and OTF synthesis flexibility of sequential measurements by employing a hybrid sampling approach where a small number of relatively wide frequency bands is measured sequentially (note from Figure 7c that a ~ 1 mm depth of field can be attained with a measurement bandwidth of ~ 2 MHz).

As we have already discussed, the synthetic 1D OTFs for sequential and frequency-multiplexed Fourier sampling derived thus far may be employed in reconstructing a filtered 1D projection of the object. We will now consider the synthesis of 2D and 3D OTFs that can be used to characterize the measurement of the entire two- or three-dimensional object using FAST.

4.3 Multi-Dimensional OTF Synthesis

Since FAST is capable of independently measuring distinct Fourier slices (and in the case of sequential sampling, even distinct Fourier coefficients) with low cross-talk by re-orienting the object or the illumination, the 2D or 3D OTF may be synthesized by combining multiple 1D OTFs over a range of projection angles and interpolating to account for sparse coverage of Fourier space, as illustrated in Figure 8. The synthetic 2D OTF can be expressed mathematically as:

$$H_{2D}(k_x, k_y; z) = W_{2D}(k_r) \sum_{\theta=0}^{\pi} H_{1D}(k_r v_0; z; \theta), \tag{22}$$

so that

$$\int_{-\infty}^{\infty} \mathcal{F}_{x,y}\left\{|\gamma_i(x, y; z)|^2\right\} dz = \int_{-\infty}^{\infty} H_{2D}(k_x, k_y; z) \mathcal{F}_{x,y}\left\{|\gamma_o(x, y; z)|^2\right\} dz, \tag{23}$$

where we have employed the mapping $\Omega_m \mapsto k_r v_o$. Here $\theta = \arcsin(k_y/k_x)$ is the Fourier slice angle, $k_r = \sqrt{k_x^2 + k_y^2}$ is the Fourier-domain radial coordinate, and $W_{2D}(k_r)$ is a radially-dependent interpolation weighting filter that has the form of a ramp function to account for the linearly-increasing spacing between the radial slices as a function of frequency [2]. Note that when the thickness of the object is much smaller than the depth of field (as in the case of sequential sampling, for example), integration along the z axis is unnecessary.

The same concept can be applied to synthesize the 3D OTF, however in the case of frequency-multiplexed sampling this is possible only if the z-dependence of the 1D OTF can be neglected (e.g. by employing a hybrid time/frequency multiplexing approach or by ensuring that the beat frequencies are non-redundant as in Figure 5d). In this case the synthetic 3D OTF can be represented mathematically by introducing a 3D radial coordinate, $k_\rho = \sqrt{k_x^2 + k_y^2 + k_z^2}$, an elevation angle, $\phi = \arcsin(k_r/k_z)$, and the 3D weighting factor, $W_{3D}(k_\rho)$, which will vary quadratically with the cross-section of the solid angle in Fourier space attributed to each slice (assuming equal angular spacing between slices):

$$H_{3D}(k_x, k_y, k_z) = W_{3D}(k_\rho) \sum_{\phi=0}^{\pi} \sum_{\theta=0}^{\pi} H_{1D}(k_\rho v_0; \theta; \phi), \tag{24}$$

such that

$$\begin{aligned} &\mathcal{F}_{x,y,z}\left\{|\gamma_i(x,y,z)|^2\right\} \\ &\quad = H_{3D}(k_x, k_y, k_z)\mathcal{F}_{x,y,z}\left\{|\gamma_o(x,y,z)|^2\right\}. \end{aligned} \tag{25}$$

Hence, as illustrated in Figure 8, by electronically programming $H_{1D}(k_{rho} v_0)$ for each orientation of the illumination with respect to the object, it is possible to dynamically synthesize slice-by-slice 2D or 3D OTFs with complicated, radially asymmetric shapes that can be tailored for specific measurement speed and sensitivity requirements, sensing tasks, and classes of objects with *apriori*-known Fourier structure such as thin cellular membranes or grid-based semiconductor structures, enabling a form of compressive imaging. Moreover, in conjunction with a feedback system, one can envision dynamic correction of coarse phase errors in the pupil function (e.g. due to flexing of a large reflector). The main constraints on the synthetic OTF are that it must possess inversion symmetry and must be representable as a sum of 1D autocorrelations. In the case of sequential Fourier sampling, each autocorrelation term corresponds to a single Fourier sample, rather than a Fourier slice, thereby offering even greater flexibility in defining the multi-dimensional OTF.

4.4 OTF for Scattering Amplitude Objects

Although in the preceding derivation we assumed a fluorescent object, FAST can also be used to measure reflective and transmissive amplitude structures (we are also developing an implementation of FAST for quantitatively measuring phase objects that will be described in a future publication). We can show, for example, that when substantially all of the scattered light is collected onto the detector, FAST can be described using the same formalism as in the case of a fluorescent object (the scattering object can be considered as an intensity mask placed in front of the detector surface). This equivalence is also approximately valid when a large portion of the scattered light is collected using a typical microscope objective, for example.

It may at first be surprising that although we have assumed coherent illumination in the preceding derivation and extended it to scattering objects, the OTF has the form of an autocorrelation, which is characteristic of an *incoherent* optical system linear in *intensity.* One interesting consequence is that speckle noise due the fine-scale structure of scattering objects is averaged out and does not contribute to the synthesized image. Furthermore, because the spatial frequency content of the illumination pattern is invariant with optical wavelength (neglecting wavelength-dependent Bragg diffraction efficiency), a FAST

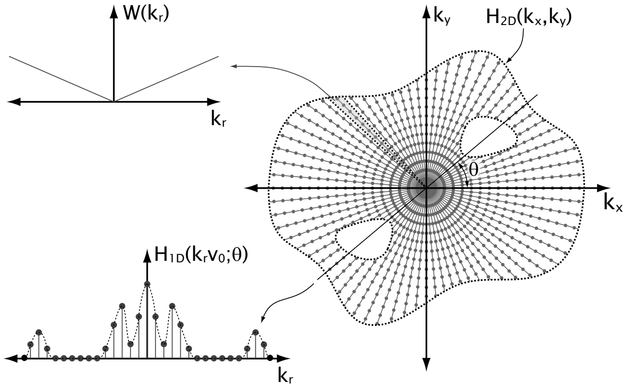

Figure 8. A complex 2D OTF with inversion symmetry can be synthesized by combining multiple rotated 1D OTFs obtained by rotating the illumination with respect to the object. Each 1D OTF may be synthesized as a continuous autocorrelation function or may be synthesized sequentially from discrete Fourier samples. An interpolating ramp filter $W(k_r)$ is applied to compensate for radially-increasing inter-sample spacing. As an example, in this way it is possible to synthesize a 2D OTF that is radially asymmetric and has missing regions as illustrated.

system using a *broadband* source such as a femtosecond laser, can be characterized by the same OTF as a monochromatic system.

5 Experimental System and Initial Results

Figure 9a shows the key elements of a proof-of-concept system built as a testbed for the RF electronics, optics and algorithms needed to implement FAST. As a retrofit to a conventional microscope, the system employs an objective lens to project acousto-optically synthesized patterns onto the object and to collect the fluoresced or scattered light onto a high-speed large-area photodiode. A retro-reflecting prism on a rotation stage is used to rotate the illumination pattern and acquire additional Fourier slices. In implementing a sequential Fourier sampling scheme, a double-sided chirp signal is applied to the Bragg cell for each slice, producing a modulated detector signal. The magnitude and phase of the Fourier slice is determined by the envelope and phase of the carrier signal, respectively. In the top inset in Figure 9a the detector signal shows the fundamental and harmonic frequencies of an amplitude grating target. Figure 9d shows two-dimensional image reconstructions obtained using the filtered backprojection algorithm as an Air Force resolution target is moved axially through a distance of $\sim$4 mm. For each image, 500 Fourier slices covering 180° were acquired with a measurement time of $\sim$10 ms per slice (we expect to speed up the measurement by several orders of magnitude in future systems implementing non-mechanical illumination rotation). Group 7 of the resolution target containing $\sim 2\ \mu$m features can be resolved throughout the 4 mm range, demonstrating a 1000-fold improvement compared to the $\sim 6\ \mu$m DOF of the 0.4 NA objective used to acquire the image. The experimental system used to obtain these results is further detailed below.

5.1 Generating the Structured Illumination

Figure 9a shows only the salient components of the Proof-of-Concept FAST system. In practice, we use a spatially-filtered DPSS CW laser (Compass 315M-100, Coherent Technologies), emitting $\sim$25 mW at 532 nm, as the light source. The horizontally-polarized collimated beam is expanded to a 12.5 mm diameter and focused in one dimension using a 200 mm focal length cylindrical lens. The focal line intercepts only the main acoustic lobe within the Bragg cell, resulting in a spatially-homogeneous diffraction. The diffracted

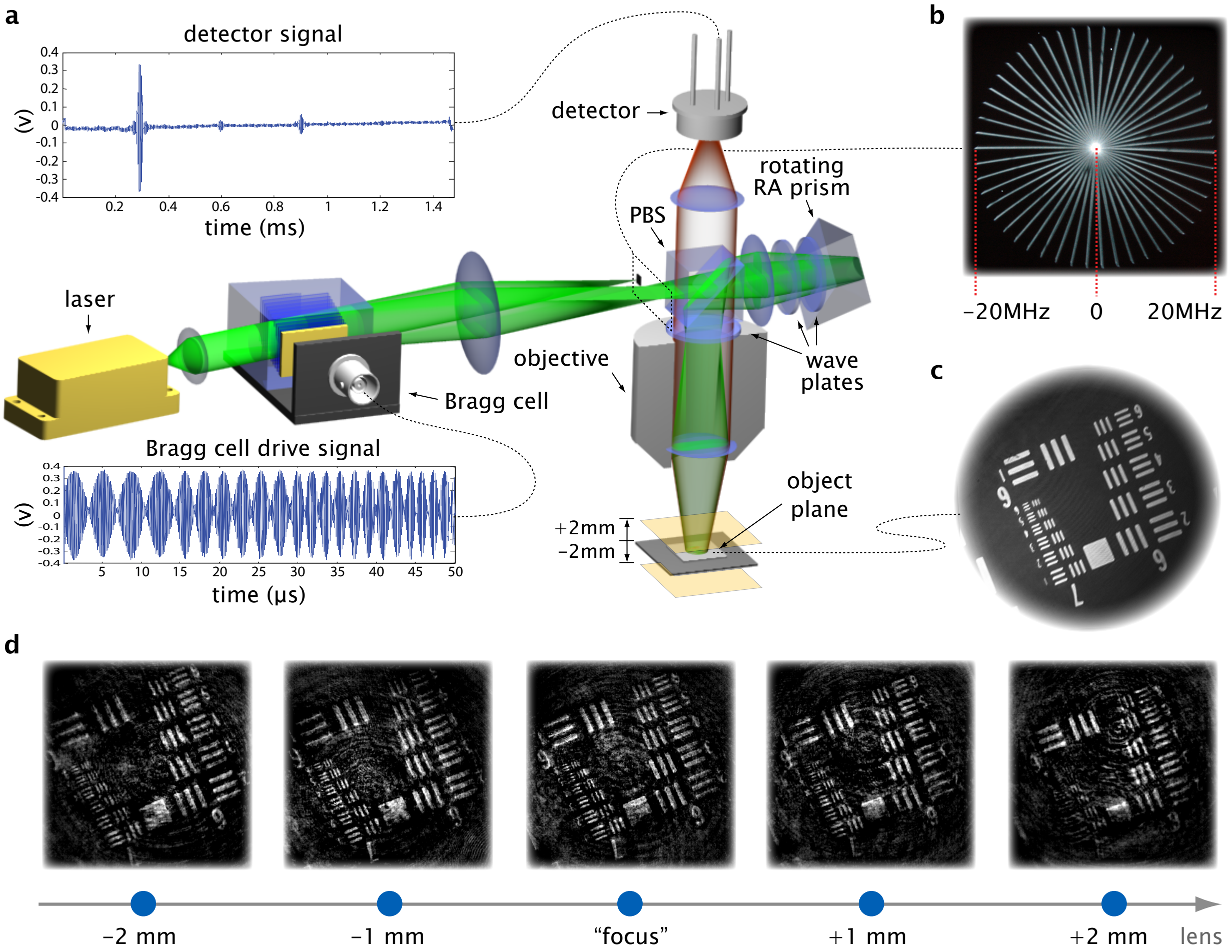

Figure 9. **(a)** Key elements of the Proof-of-Concept (PC) FAST system. A double-sided RF chirp applied to the Bragg cell sweeps two 1st-order diffracted beams, which interfere at the sample. A fast detector measures the sample's response. A mechanized right-angle prism rotates the illumination (see also Supplemental Information Animation 1). **(b)** Swept-frequency sampling of the Fourier plane for 25 illumination rotation prism orientations as imaged by a CCD camera. **(c)** A conventional dark-field image of an Air Force resolution target using the PC-FAST objective. **(d)** Reconstructions of the AF resolution target using filtered backprojection as a function of defocus. The entire Group 7 is resolved throughout the 4mm axial range, illustrating the large depth of field attainable with FAST. The circular artifacts in the reconstructions are due to back-reflections in the optical system and are expected to be suppressed when all surfaces are anti-reflection coated.

light is retro-reflected and re-collimated using the same cylindrical lens. A 4f telescope is used to block the undiffracted light and to de-magnify (by a factor of 0.6) and relay the diffracted field onto the wavefront rotator, which is located at a conjugate plane of the Bragg cell. A polarizing beam splitter (PBS) in the telescope path is used as a passive optical isolator, sending the vertically-polarized 1^{st} order diffracted light to the wavefront rotator. The wavefront rotator comprises a retro-reflecting knife-edge prism (Optosigma 055-0280) mounted on a fast motorized rotation stage (Micos DT-80R) capable of 6.25 revolutions per second (which translates to 25 complete Fourier slice revolutions per second). We use a retro-reflecting prism (instead of a dove prism) due to its minimal optical aberrations and relative ease of alignment [28]. An arrangement of stationary and rotating waveplates placed between the prism and the PBS is used to change the polarization of retro-reflected light to horizontal and compensate for polarization rotation [29]. After passing through the PBS, the rotated illumination is routed through a custom-built microscope and a 20x 0.4 NA objective (Nikon M-PLAN ELWD) onto the object, which is also located approximately in a conjugate plane of the Bragg cell. The microscope contains additional waveplates and polarizing beam splitters to maximize light throughput and includes optical paths for a Fourier-plane CCD camera used for alignment (Figure 9b) and a reference photodiode used to suppress intensity noise. The system also includes an Acousto-Optic Modulator (AOM) (Crystal Technology 3350-120) placed after the laser, making it possible to “freeze” the running fringes illuminating the object by strobing the light at the the two-tone beat frequency [34]. In the end, accounting for the inefficiencies of the AOM, Bragg cell, and the optical path, about ∼1 mW or ∼4% of the light from the laser is delivered to the object, covering a field-of-view ∼500 μm in diameter. The Bragg cell (NEOS AOBD45050-15-6.5deg) is an acoustically-rotated slow-shear TeO_2 device ($v_s \sim 0.66$ mm/μs) with a bandwidth of ∼40 MHz, resulting in a time-bandwidth product of ∼800 and a minimum demagnified fringe period of ∼1.25 μm at the target, a measure of the maximum resolution of the proof-of-concept system.

5.2 Electronic Pattern Synthesis

PC-FAST relies on Direct Digital Synthesis (DDS) electronics to generate RF signals, achieving 32-bit frequency, 14-bit phase and 10-bit amplitude resolution as well as accuracy and stability that depend only on the characteristics of the clock source. Although DDS technology is precise, agile and inexpensive, it limits the RF signals to CW or swept tones. Future implementations of FAST based on frequency-multiplexed Fourier sampling will require programmable arbitrary waveform synthesis. The swept two-tone drive signal is synthesized by current-summing two outputs from a computer-controlled 4-channel DDS board (modified Analog Devices AD9959 evaluation board) and amplified (using a Minicircuits ZHL-2-8 amplifier) to a level of ∼60 mW, well below the power needed to achieve maximum diffraction efficiency (∼800 mW), in order to maintain a linear acousto-optic response. The third DDS channel is used to automatically reset the sweep and to trigger the digitizer. For the reconstructions shown in Figure 9d the DDS board was programmed to sweep the two-tone beat frequency between 10 kHz and 20 MHz with 10 kHz frequency steps over ∼2 ms for each slice. Custom Labview software is used to control the DDS, the rotation stage, as well data acquisition and processing, automating the entire measurement.

5.3 Heterodyne Detection

The object’s response to the moving illumination pattern is measured using a custom-built autobalancing differential detector, in order to suppress relative intensity noise. Based on design considerations described by P. Hobbs [35, 36], this detector uses transistor “bootstrapping” to achieve a bandwidth of ∼70 MHz using two large-area photodiodes (Hamamatsu S1722-01), has a noise-equivalent power of 5 $\mathrm{pW}/\sqrt{\mathrm{Hz}}$, and can be tuned to attain ∼70 dB of noise cancellation at low frequencies. The comparison signal for differential cancellation is split-off from the illumination via one of the PBS ports in the microscope and can be intensity-tuned by adjusting a waveplate. The differentially detected signal is mixed using an analog multiplier (Analog Devices AD835) with a local oscillator signal offset by 50 kHz and swept synchronously with the two-tone beat frequency using the fourth DDS channel, filtered by a 50 kHz bandpass filter, and digitized at 1 MHz using a USB oscilloscope (Cleverscope CS328A) synchronously with the DDS clock. This electronic heterodyne detection scheme not only reduces the number of digital samples needed to measure a Fourier slice from $\mathcal{O}(N^2)$ to $\mathcal{O}(N)$, but also lowers the noise bandwidth by a factor of N, where N is the number of resolvable frequencies per slice (or equivalently, half the time-bandwidth product of the Bragg cell).

6 Conclusions

While the initial results shown in Figure 9d prove the basic concepts and algorithms of FAST, they represent only the first steps towards a versatile computational imaging technique. In the near future we hope not only to improve the image quality, but also to demonstrate some of the other capabilities in the FAST toolbox, including imaging of fluorescent biological samples, high-NA large-working-distance imaging without precision optics, dynamic filtering and aberration compensation, and three-dimensional Fourier synthesis. We are also investigating a next generation FAST system based on a pulsed laser source implementing a non-mechanical illumination rotation scheme with the potential to measure as many as 10^8 Fourier samples per second. Pulsed FAST could also be used for multi-photon imaging and combined with other time-resolved imaging modalities, such as fluorescence lifetime imaging [37] and time-gated techniques for imaging in scattering media [38]. The capabilities of FAST are well suited for studying dynamic processes in the sample volume. High-speed wide-field imaging, large DOF, Fourier-selectivity, and coherence-gating of broadband FAST, could, for example, enable real-time tracking of neuron signals propagating along multiple volume-distributed dendrites using voltage-sensitive fluorescent dyes [39]. A reflective lensless implementation of FAST could be suitable for high-resolution imaging in FIR, UV, and X-ray regimes, where precision optics and dense detector arrays pose a technological challenge. Other applications of FAST may include dynamic characterization of Micro Electro Mechanical Systems [40] and even near-field Fourier-domain imaging [41].

7 Acknowledgments

Supported by the Laboratory Directed Research and Development program at Sandia National Laboratories. Sandia is a multiprogram laboratory operated by Sandia Corporation, a Lockheed Martin Company, for the United States Department of Energy's National Nuclear Security Administration under Contract DE-AC04-94AL85000. We would also like to acknowledge the NSF IGERT OSEP and COSI Fellowships, and the NASA ROSES PIDD grant program for funding this research. D. Feldkhun is also indebted to M. Mermelstein for many inspiring discussions related to this work during their collaboration at MIT.

8 References

[1] E. N. Leith and J. Upatnieks, "Reconstructed wavefronts and communication theory," J. Opt. Soc. Am. **52**, 1123–1130 (1962).

[2] A. C. Kak and M. Slaney, *Principles of Computerized Tomographic Imaging* (IEEE Press, New York, 1988).

[3] J. R. Fienup, "Lensless coherent imaging by phase retrieval with an illumination pattern constraint," Optics Express **14**, 498–508 (2006).

[4] M. G. L. Gustafson, "Surpassing the lateral resolution limit by a factor of two using structured

illumination," J. Microscopy **198**, 82–87 (2000).

[5] J. García, Z. Zalevsky, and D. Fixler, "Synthetic aperture superresolution by speckle pattern projection," Optics Express **13**, 6073 (2005).

[6] M. F. Duarte, M. A. Davenport, D. Takhar, J. N. Laska, T. Sun, K. F. Kelly, and R. G. Baraniuk, "Single-pixel imaging via compressive sampling," IEEE Signal Proc. Mag. pp. 83–91 (2008).

[7] G. Indebetouw, P. Klysubun, T. Kim, and T. C. Poon, "Imaging properties of scanning holographic microscopy," J. Opt. Soc. Am. A **17**, 380–390 (2000).

[8] D. Feldkhun and K. Wagner, "Fourier analysis and synthesis tomography: A structured illumination approach to computational imaging," in "Computational Optical Sensing and Imaging (COSI) Conference," (OSA, 2007).

[9] D. Feldkhun and K. Wagner, "Fourier analysis and synthesis tomography: high-resolution long-range volume imaging of cells and tissue," in "Biomedical Optics Conference," (OSA, 2008).

[10] D. Feldkhun and K. Wagner, "Fourier analysis and synthesis tomography: dynamic measurement of 2d and 3d structure," in "Novel Techniques in Microscopy Conference," (OSA, 2009).

[11] N. Streibl, "Three-dimensional imaging by a microscope," J. Opt. Soc. Am. A **2**, 121–127 (1985).

[12] H. Gross, ed., *Handbook of Optical Systems, Vol. 2* (WILEY-VCH, Weinheim, Germany, 2005).

[13] E. Abbe, "Beiträge zur theorie des mikroskops and der mikroskopischen wahrnehmung," Arch. mikrosk. Anat. EntwMech **9**, 413 (1873).

[14] W. E., "Three-dimensional structure determination of semi-transparent objects from holographic data," Opt. Commun. **1**, 153–156 (1969).

[15] J. W. Goodman, *Introduction to Fourier Optics* (McGraw-Hill, New York, 1996), 2nd ed.

[16] R. A. Hutchin, "Microscope for producing high resolution images without precision optics," U.S. Patent No. 4,584,484 (1986).

[17] T. M. Turpin, "Image synthesis using time sequential holography," U.S. Patent No. 5,751,243 (1998).

[18] N. D. Ustinov, A. V. Anufriev, A. L. Volpov, Y. A. Zimin, and A. Tolmachev, "Active aperture synthesis in observation of objects via distorting media," Sov. J. Quantum Electron. **17**, 108–110 (1987).

[19] V. I. Mandrosov, *Coherent Fields and Images in Remote Sensing* (SPIE Press, Bellingham, WA, 2003).

[20] J. Ryu, S. S. Hong, K. P. Horn, D. F. Freeman, and M. S. Mermelstein, "Multibeam interferometric illumination as the primary source of resolution in optical microscopy," Appl. Phys. Lett. **88**, 171112 (2006).

[21] J. Ryu, "Resolution improvement in optical microscopy by use of multi-beam interferometric illumination," Ph.D. thesis, MIT (2003).

[22] M. S. Mermelstein, "Synthetic aperture microscopy," Ph.D. thesis, MIT (1999).

[23] M. S. Mermelstein, "Multiple beam pair optical imaging," U.S. Patent No. 6,016,196 (2000).

[24] P. Hobbs and G. S. Kino, "Generalizing the confocal microscope via heterodyne interferometry and digital filtering," J. Microscopy **160**, 245–264 (1990).

[25] A. VanderLugt, *Optical Signal Processing* (Wiley-Interscience, 1992).

[26] S. H. Hong, M. S. Mermelstein, and D. M. Freeman, "Reflective acousto-optic modulation with surface acoustic waves," Applied Optics **43**, 2920–2924 (2004).

[27] D. M. Bloom, "The grating light valve: revolutionizing display technology," in "Proc. SPIE," , vol. 3013 (SPIE, 1997), vol. 3013, p. 165.

[28] D. W. Swift, "Image rotation devices- a comparative survey," Opt. Laser Technol. **4**, 175–188 (1972).

[29] D. W. Swift, "Rotation prisms in series," Opt. Laser Technol. **18**, 213–215 (1986).

[30] A. E. T. Chiou and P. Yeh, "Scaling and rotation of optical images using a ring cavity," Applied Optics **29**, 1584–1586 (1990).

[31] S. J., U. Ahlgren, T. Perry, B. Hill, A. Ross, J. Hecksher-Sorensen, R. Baldock, and D. Davidson, “Optical projection tomography as a tool for 3d microscopy and gene expression studies,” Science **296**, 541–545 (2002).

[32] J. P. Xu and R. Stroud, *Acousto-optic devices: principles, design, and applications* (Wiley-Interscience, 1992).

[33] R. B. Blahut, *Theory of Remote Image Formation* (Cambridge University Press, Cambrisge, UK, 2004).

[34] S. M. Mermelstein, D. F. Feldkhun, and L. G. Shirley, “Video-rate surface profiling with acousto-optic accordion fringe interferometry,” Opt. Eng. **39**, 106–113 (2000).

[35] P. Hobbs, “Ultrasensitive laser measurements without tears,” Applied Optics **36**, 903–920 (1997).

[36] P. Hobbs, *Building Electro-Optical Systems: Making It All Work* (John Wiley and Sons, 2000).

[37] D. Elson, S. Webb, J. Siegel, K. Suhling, D. Davis, J. Lever, D. Phillips, A. Wallace, and P. French, “Biomedical applications of fluorescence lifetime imaging,” Optics and Photonics News **13**, 26–57 (2002).

[38] C. Dunsby and P. M. W. French, “Techniques for depth-resolved imaging through turbid media including coherence-gated imaging,” J. Phys. D: Appl. Phys. **36**, R207–R227 (2003).

[39] M. Atsushi, “Innovations in the imaging of brain functions using fluorescent proteins,” Neuron **48**, 189–199 (2005).

[40] W. Hemmert, M. S. Mermelstein, and D. M. Freeman, “Nanometer resolution of three-dimensional motions using videointerference microscopy,” in “Twelfth IEEE International Conference on Micro Electro Mechanical Systems, 1999. MEMS ’99.”, (SPIE, 1999), pp. 302–308.

[41] G. E. Cragg and P. T. C. So, “Lateral resolution enhancement with standing evanescent waves,” Optics Letters **25**, 46–48 (2000).

1	MS1411	M.B. Sinclair 01816
1	MS1082	F.B. McCormick 01727
1	MS0359	Y.V. Moreno 01912
1	MS0359	D.L. Chavez 01911
1	MS0899	Technical Library 09536(electronic copy)

Sandia National Laboratories